npj | climate and atmospheric science

Article

Published in partnership with CECCR at King Abdulaziz University

https://doi.org/10.1038/s41612-025-01293-5

Tracing South Asian monsoon variability through a late miocene record from the himalayan foreland basin

Mohd Munazir Chauhan[1,2], Sajid Ali[3] ✉, Ali M. Khan[4] ✉, Pankaj Kumar[5], Madhav K. Murari[5], Pujarini Samal[6], Birendra P. Singh[2], Vikas Adlakha[7], Leema Saikia[5], Binita Phartiyal[1] & Anupam Sharma[1]

The relative contributions of global cooling and tectonic forcing to the reorganization of the South Asian monsoon during the critical Late Miocene remain poorly constrained. By analyzing sedimentological and geochemical proxies from the Tanakpur-Sukhidang section in the Himalayan foreland basin, we reconstruct paleoclimatic conditions to infer South Asian monsoon variability during this period. The enrichment of LREEs, a flat HREEs pattern and a negative Eu anomaly, along with elemental ratios of La/Sc and Th/Co, suggest a persistent felsic source derived from the Himalaya since ~12 Ma. Clay mineral variations, particularly the shift in smectite content and smectite/(illite + chlorite) ratio, together with geochemical weathering indicators (CIA, WIP and Rb/Sr), document a relative increase in chemical weathering around 8 Ma. These mineralogical and geochemical transformations are synchronous with widespread indicators of South Asian monsoon weakening linked with change in exhumation rate of the Himalayan-Tibetan Plateau and Late Miocene global cooling. Where reduced physical erosion and enhanced sediment-water interaction under cooler and more seasonal conditions amplified chemical weathering feedbacks. Together, these processes reorganized regional hydrology and monsoon dynamics, underscoring the coupled influence of tectonics and global climate forcing in driving the Late Miocene weakening of the South Asian monsoon. However, the relative influence of climate versus tectonics still remains inherently very complex and higher resolution provenance data, thermochronology and climate model simulations will be crucial for fully understanding the mechanisms underlying the Late Miocene Change.

The paleogeography and topography of Asia underwent dramatic changes during the Cenozoic due to the India-Asia collision, driven by the progressive uplift of the Himalayan-Tibetan Plateau (HTP), which began approximately 50–60 Ma ago[1,2]. The uplift of the HTP and the associated reorganization of Asian topography profoundly influenced the formation and evolution of the Asian monsoon system[1,3–5]. Meanwhile, global climate entered a long-term cooling trajectory beginning in the Eocene[6]. In Asia, paleoenvironmental conditions transitioned from circulation dominated by planetary winds to a monsoon-controlled regime during the Late Oligocene-Early Miocene (ca. 23 Ma)[7,8]. Although the South Asian monsoon, also called as Indian monsoon, is believed to have initiated around 9-8 Ma ago[9], with early signs of development during the Early Miocene[10] and even evidence dating back to the Eocene[11], its strengthening and climatic significance are thought to have been strongly modulated by HTP uplift beginning in the Eocene[4,12,13].

To understand monsoon variability during the Late Miocene, we conducted this study on siliciclastic sediments from the Himalayan Fold Belt, which receives a substantial sediment flux from the Northwestern (NW) Himalaya and its associated lithotectonic units[14–17]. Erosion in the NW Himalaya closely tracks monsoon intensity across tectonic and orbital timescales and is largely concentrated along the southern Himalayan flank[18]. In addition to summer monsoon rainfall, this region receives winter moisture from Westerly disturbances[19]. The western HFB is notably more seasonal relative to the wetter eastern HFB[20]. Previous regional paleoclimatic studies from the HFB provide a critical framework for linking erosion and weathering proxies with independent climatic archives[16,20–22]. However, the

[1]Birbal Sahni Institute of Palaeosciences, Lucknow, India. [2]Department of Geology, Panjab University, Chandigarh, India. [3]Department of Environmental Science, Jamia Millia Islamia, New Delhi, India. [4]Springer Nature Group, Heidelberg, Germany. [5]Inter-University Accelerator Centre, New Delhi, India. [6]CSIR-National Botanical Research Institute, Lucknow, India. [7]Wadia Institute of Himalayan Geology, Dehradun, India. ✉e-mail: asajid2@jmi.ac.in; drikhan@protonmail.com

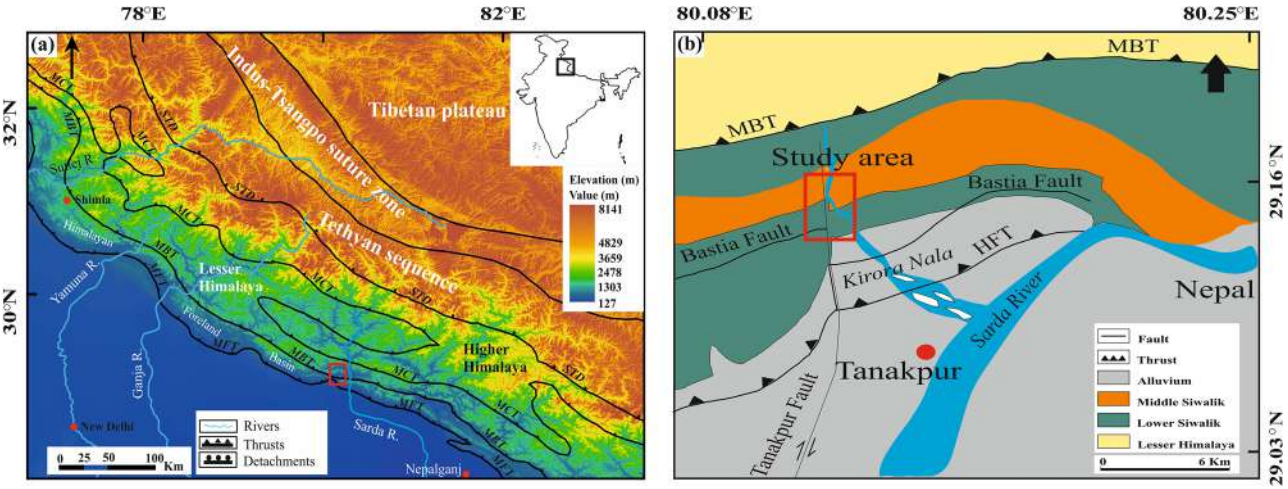

Fig. 1 | The location of the study area and related region. a Digital elevation map of NW Himalaya; **b** geological map of the HFB of NW Himalaya.

mechanistic drivers of the Late Miocene climatic shift remain debated, with hypotheses invoking either HTP uplift[13,23] or long-term global cooling[24,25]. To test these hypotheses requires a robust characterization of paleoclimatic trends in the HFB, particularly the evolution of the South Asian monsoon, which serves as a crucial archive for disentangling climate-tectonic linkages.

Owing to its pivotal role as a repository of monsoonal and tectonic signals, the geological framework of the HFB requires careful consideration. The basin developed during the Paleogene as a result of the Indian plate bending downward in response to the tectonic pressures from the collision between India and Asia along the northern edge of the Himalayas[26–28]. The basin is bounded by the Himalayan Frontal Thrust (HFT) to the south and the Main Boundary Thrust (MBT) to the north (Fig. 1a). The basin extends more than 2000 km from the Potwar plateau in Pakistan to Arunachal Pradesh in India. Covering an area of 30,300 km², it is the largest terrestrial basin, with elevations ranging from 1800 to 2700 m. Climatically, the basin is situated at the intersection zone between the Southwest monsoon and the complex orography of the HTP. The Paleogene Sub-Himalaya basin sediments are exposed in regions such as Kashmir-Hazara, Salt Range, Jammu (Mandi and Kalakot), Himachal Pradesh, Darjeeling and Arunachal Pradesh[29,30]. The Neogene sediments are consistently exposed along the entire basin, referred to as the Siwalik Group. The Siwalik Group, ~7 km thick, is subdivided based on faunal and sedimentological criteria into three units: the mudstone-rich Lower Siwalik (Early Miocene), sandstone-dominated Middle Siwalik (Late Miocene) and gravelly Upper Siwalik (Late Miocene-Pleistocene)[31,32].

This study presents a continuous record of clay mineral assemblages integrated with the geochemical compositions of major, trace and rare earth elements (REEs) in siliciclastic sediments from the HFB between 12.5 and 4 Ma. The objectives are twofold (1) to constrain the provenance and compositional characteristics of the source rocks supplying these sediments and (2) reconstruction of paleoweathering patterns and South Asian monsoon evolution to evaluate their relationship to HTP uplift and global cooling during the Late Miocene.

Results

Major elements

The major element concentrations of the studied samples of the Tanakpur-Sukhidang (TS) section are given in Supplementary Table 1 and plotted in Fig. S1a. The major oxide composition is dominated by high concentrations of SiO_2 and Al_2O_3, with SiO_2 ranging from 56.67 to 77.63% (ave. 67.50%) and Al_2O_3 from 12.42 to 18.61% (ave. 15.40%). Among the other oxides, TiO_2 ranges between 0.45 and 0.73% (ave. 0.59%), Fe_2O_3 from 1.54 to 5.76% (ave. 3.71%) and MnO remains low, varying from 0.01 to 0.04% (ave. 0.02%). The contents of MgO and CaO range from 0.44 to 2.22% (ave. 1.30%) and 0.19 to 0.26% (ave. 0.21%), respectively. Alkali oxides also show moderate variability, with Na_2O ranging from 0.21 to 0.69% (ave. 0.45%) and K_2O from 1.02 to 3.34% (ave. 2.23%). P_2O_5 is present in minor amounts, ranging from 0.03 to 0.11% (ave. 0.04%). The values of Loss on ignition (LOI) range from 6.28 to 14.54% (ave. 10.25%). The major oxide ratio of SiO_2/Al_2O_3 varies from 0.17 to 0.29 (ave. 0.23), Na_2O/Al_2O_3 varies from 0.01 to 0.05 (ave. 0.03) and K_2O/Al_2O_3 varies from 0.08 to 0.21 (ave. 0.14) (Fig. S2a–c). The calculated CIA[33] and WIP[34] values, based on major element concentrations, range from 77.84 to 83.94 (ave. of 81.40) and from 17.08 to 38.55 (ave. 27.22), respectively (Supplementary Table 1).

Trace elements

The trace element concentrations of studied samples from the TS section are presented in Supplementary Table 2 and plotted in Figure. S1b. Despite depositional age differences, all analyzed samples exhibit strong geochemical similarity, with only minor variations. The concentrations of the highly compatible transition trace elements (i.e., Sc, Cr, Co and Ni) vary from 6.45 to 19.67 ug/g (ave. 12.47 ug/g), 30.68 to 129.51 ug/g (ave. 71.27 ug/g), 2.94 to 19.76 ug/g (ave. 9.78 ug/g) and 8.93 to 53.76 ug/g (ave. 9.78 ug/g), respectively. Uranium (U) and thorium (Th) concentrations range from 6.96 to 26.22 ug/g (ave. 12.73 ug/g) and 1.0 to 3.79 ug/g (ave. 1.75 ug/g), respectively. The large ion lithophile elements Rb and Sr range from 93.98 to 284.02 ug/g (ave. 184.02 ug/g) and 25.60 to 63.92 ug/g (ave. 41.36 ug/g), respectively (Supplementary Table 2). The Rb/Sr ratios range from 2.64 to 7.38 (ave. 4.45) (Supplementary Table 2). The ratios of La/Sc, Th/Sc, Th/Co, Cr/Th and La/Co fall within the range of UCC[35] (Fig. S2). Th La/Sc ranges from 1.61 to 4.64 (ave. 2.86), Th/Sc from 0.64 to 1.83 (ave. 1.05), Th/Co from 0.66 to 4.85 (ave. 1.59), Cr/Th from 3.32 to 10.49 (ave. 5.74) and La/Co from 1.59 to 14.22 (ave. 4.32) (Figure. S2; Supplementary Table 2).

Rare earth elements (REEs)

The REEs data for the TS section samples are presented in Supplementary Table 3 and plotted in Fig. S1c, d. The normalized REEs distribution pattern shows a significantly enriched LREEs and depleted HREEs pattern. Additionally, the REEs pattern of chondrite-normalized UCC[35] and PAAS[36] is similar to the chondrite-normalized REEs pattern of the studied samples (Figure. S1c). In the studied section, the PAAS normalized REEs show a similar pattern and all the values are close to 1 (Fig. S1d). The concentration of REEs ranges from 85.25 to 277.21 ug/g (ave. 147.51 ug/g). The ∑HREEs and ∑LREEs varies from 75.99 to 254.74 ug/g (ave. 134.73 ug/g) and from 7.34 to 24.57 ug/g (ave. 11.87 ug/g), respectively. The Eu anomaly (Eu/Eu*) values in the studied section vary from 0.47 to 0.7 (ave. 0.60) (Figure. S2i).

Clay mineral assemblages

The XRD analysis revealed that the primary constituents of the clay minerals are illite, kaolinite and smectite, with a small amount of chlorite (Fig. 2;

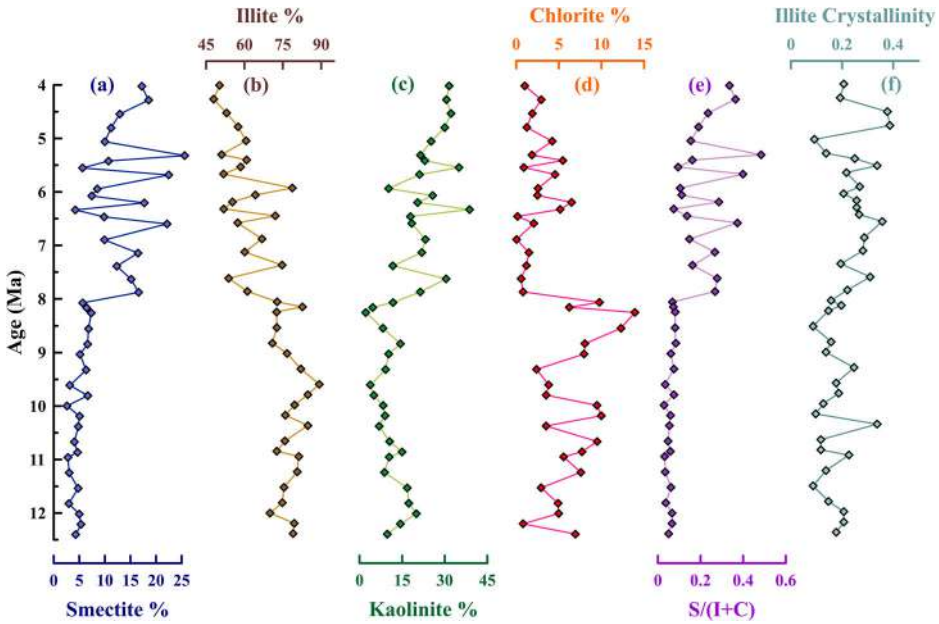

Fig. 2 | Clay mineral records of the TS section. Panels (**a–d**) show the abundances of smectite, illite, kaolinite and chlorite. Panels (**e**) and (**f**) show the smectite/(illite + chlorite) ratio and illite crystallinity, respectively.

Supplementary Table 4). The major constituents are illite and kaolinite which range from 47.95 to 89.24% (ave. 68.83%) and from 2.16 to 38.75% (ave. 17.25%), respectively. The smectite and chlorite range from 2.58 to 25.61% (ave. 9.22%) and from <1.0 to 17.93% (ave. 4.70%), respectively. The relatively high values of illite are observed from 12.5 to 8.0 Ma, followed by a sharp decline at ~ 8.0 Ma (Fig. 2b). In contrast, opposite trends are exhibited in the concentrations of smectite and kaolinite (Fig. 2a, c). The illite crystallinity index shows values ranging from 0.13 to 0.43 (ave. 0.25) and exhibit a similar trend as kaolinite and smectite (Fig. 2f).

Discussion

Constraining sediment provenance is essential prior to interpreting weathering records and paleoclimate reconstructions based on clay mineral assemblages and geochemical compositions. Previous studies have emphasized that variations in source lithology or shifts in sediment provenance can significantly influence clay mineral abundances and sediment geochemistry, potentially obscuring primary climatic signals[16,36–40]. To a certain extent, tectonic activity can alter sediment provenance potentially masking or overprinting the weathering and climate signals recorded in clay minerals and geochemical compositions[41].

The geochemical composition of siliciclastic sediments is widely recognized as a reliable approach for determining provenance and source rock composition[21,42–44]. REEs along with certain trace elements (e.g., Th, Co, Sc and Cr) are particularly effective for differentiating felsic from mafic sources because of their relative stability during sedimentary processes such as weathering, erosion and diagenesis[45–49]. Furthermore, REEs pattern and europium anomaly (Eu/Eu*) values provide critical insights into source rock composition[46]. Sediments derived from felsic sources typically exhibit high LREE/HREE ratios and a pronounced negative europium anomaly, whereas those from mafic sources are characterized by lower LREE/HREE ratios and a positive europium anomaly[43]. The chondrite-normalized REEs pattern of the analyzed samples displays LREEs enrichment and HREEs depletion, closely resembling the PAAS distribution pattern, indicating derivation predominantly from felsic source rocks in the Himalayas (Figure. S1c). PAAS-normalized REEs pattern reveal similar trends, supporting sediments origin from the felsic source rocks (Figure. S1d). The Eu/Eu* versus Th/Sc scatter plot (Fig. 3a) further confirms a felsic source for the TS sediments. Additional geochemical parameters have been used to assess sediment provenance[47–49]. In clastic sedimentary rocks, REEs are relatively immobile during sedimentary processes and thus serve as effective indicators of source rock composition. The bivariate plot of La/Sc versus Th/Co is also a useful tool for interpreting source rock characteristics in clastic sediments[50]. For the analyzed TS samples, this plot indicates derivation of the sediments from felsic source rocks as well (Fig. 3b). Similarly, the La-Th-Sc ternary diagram effectively constrains source rock composition[43], with most samples clustering within the felsic field, corroborating the felsic origin (Fig. 3c). Elemental ratios such as La/Sc, Th/Sc, Th/Co, Cr/Th and La/Co further constrain source lithology[43]. These ratios fall within the range typical of felsic-derived sediments and are comparable to UCC values[35], supporting the inference of a dominant felsic source for the TS sediments between 12.5 to 4 Ma (Fig. S2). The temporal variations in La/Sc, Th/Sc, Th/Co, Cr/Th, La/Co and Eu/Eu* between the 12.5-4 Ma interval are plotted in Supplementary Fig. S2. These records display a subtle inflection near ~8 Ma, which may correspond to the initial surface exposure of the Inner Lesser Himalaya and a consequent, though limited, increase in its sedimentary contribution. This subtle shift did not modify the overall felsic geochemical signature of the detritus, consistent with isotopic evidence from the Bengal Fan and Siwalik successions. Derry and France-Lanord[51] also suggest that the detrital supply remained essentially stable throughout the Neogene. However, a pronounced rise in riverine Sr isotopic ratios during the Late Miocene was attributed to the progressive unroofing and erosion of metamorphosed carbonate (metalimestone) units within the central Himalaya, rather than to any major change in sediment source region[52]. These findings support our geochemical interpretation that the observed variability reflects a minor compositional adjustment within the Himalayan source terranes. To further assess the extent to which the TS sediments retain their primary source characteristics, bivariate plots of immobile element ratios, such as Al_2O_3/SiO_2 vs. Fe_2O_3/SiO_2 are also used[53]. Data from the Higher Himalaya, Lesser Himalaya and Siwalik sediments are plotted alongside our dataset for comparison[51]. Comparative fields indicate that most of the sediments originated dominantly from variable contributions from the Higher Himalaya with minor inputs from the Lesser Himalaya and Siwalik source regions[52] (Fig. 3d). This shows that the TS sediments retain the geochemical fingerprint of their source terranes. The analysis of Late Neogene sandstones from the same region, based on variations in texture, petrography and mineral composition, indicates the Higher Himalaya as the dominant sediment source, with minor contributions from the Lesser Himalaya, thereby supporting our findings[15,54,55]. Additional records of the geochemical composition of major oxides and REEs in Siwalik sediments similarly identify felsic rocks, derived from the Higher and Lesser Himalayas, as the primary

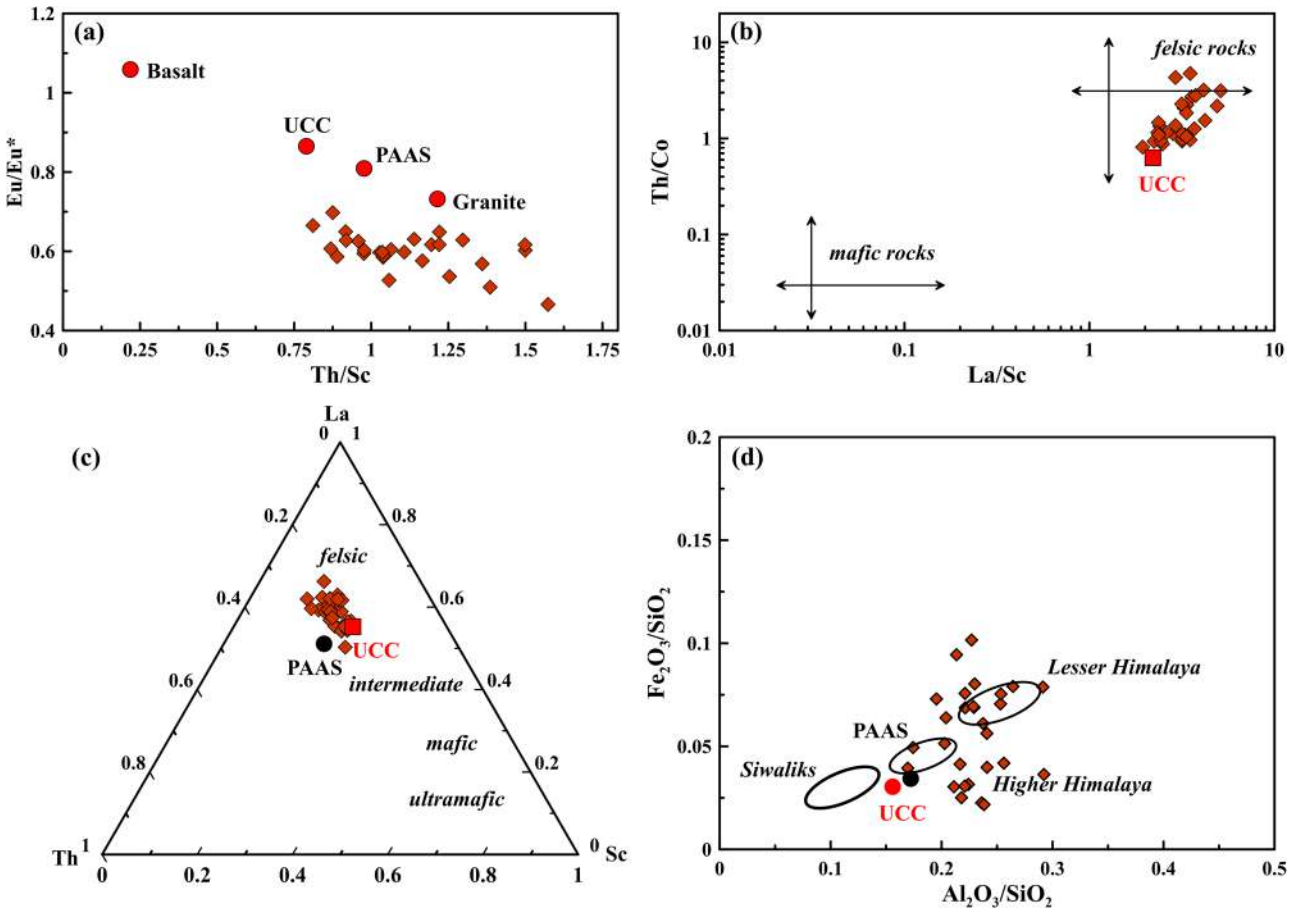

Fig. 3 | Binary and ternary geochemical relationships constraining provenance. a The scatter plot of Eu/Eu* vs. Th/Sc; **b** scatter plot of Th/Co vs. La/Sc; **c** the ternary plot of La-Th-Sc; and **d** scatter plot of Fe_2O_3/SiO_2 vs. Al_2O_3/SiO_2 of the TS section sediments and endmembers[53].

source[14]. Likewise, studies of paleo-weathering and provenance from the HFB in the western Himalaya indicate that the sediments were predominantly derived from Higher Himalayan rock formations, with only a minor contribution from the Lesser Himalayan Crystalline[16]. The felsic nature of the source rocks is further corroborated by heavy mineral assemblages from the Upper Siwalik Group in the Jammu region[56]. Geochemical records from the present study, combined with these previous findings, confirm that the sediments are primarily sourced from felsic lithologies, chiefly from the Higher Himalayas with minor input from the Lesser Himalayas and Siwalik. Hence, the uniform trace element compositions, consistent REEs pattern and stable source rock discrimination plots collectively point to a persistent felsic provenance between 12.5 and 4 Ma. Therefore, the observed temporal variations in weathering indices and clay mineralogy are best explained by fluctuations in chemical weathering intensity driven by monsoonal variability, accompanied by a modest increase in the sedimentary contribution from the uplifted Lesser Himalaya during this interval.

The clay mineral assemblages of the clastic sediments generally represent the chemical alteration products of the source rocks and have a direct link to climatic conditions[57]. Illite and chlorite in the clay mineral assemblage are typically produced by the physical erosion of terrestrial rocks under cold and arid climatic conditions[58]. Smectite generally forms under moderate hydrolysis and alternating wet and dry seasons, where episodic leaching and cation retention promote its stabilization[58,59]. Since the sediments originate from felsic source regions, volcanic influence is negligible, implying that smectite abundance here likely records change in monsoon intensity and climatic seasonality rather than volcanic alteration. Kaolinite, on the other hand, is formed under intense chemical weathering associated with warm and wet climatic conditions[58,59]. The clay minerals in the basin sediments can alter by diagenetic changes either soon after deposition or during burial[58,60–63]. To correctly interpret their climatic significance, it is essential to evaluate potential diagenetic alteration, as burial diagenesis can convert detrital smectite to illite and hence many alter clay mineral signature of chemical weathering intensity[58]. The diagenetic transformation of clay mineral assemblages is among the most common diagenetic processes in sedimentary basins[64] and according to the classical diagenesis model, illite content should gradually increase with rising temperature and pressure during deeper burial[65]. Two mechanisms are typically invoked: (1) smectite layers convert to illite layers via Al^{3+} and K^{+} released from K-feldspar and mica[66,67] and (2) smectite dissolves while illite recrystallizes concurrently[68,69]. The crystallinity index of illite is a key tool to distinguish detrital from diagenetic illite: illite from chemical weathering shows expanded layers due to hydrolyzation, whereas clastic origin illite exhibits good crystallinity and low index values[58]. On the contrary, illite formed via diagenesis typically exhibits a high crystallinity index. In our studied samples, the low illite crystallinity values (0.13–0.43, with an ave. of 0.25) indicate well-crystallized, detrital illite (Fig. 2f). Further, the absence of a depth-related increase in illite content (Fig. 2b) and zircon fission-track constraints showing burial temperatures below 100 °C[17] further confirm that 3000 m-thick TS section experienced minimal diagenetic alteration, preserving a true detrital weathering signal. The SEM micrographs (Fig. S3) further reveal angular morphologies and surface textures consistent with physical erosion, reinforcing the interpretation that illite was primarily derived from the erosion of source rocks rather than in-situ diagenetic processes. Therefore, these morphological features provide critical visual confirmation of the sediment's provenance and enhance the reliability of the mineralogical and geochemical weathering indicators used in this study. The resultant smectite content along with smectite/illite + chlorite (S/(I + C)) ratio, in the present

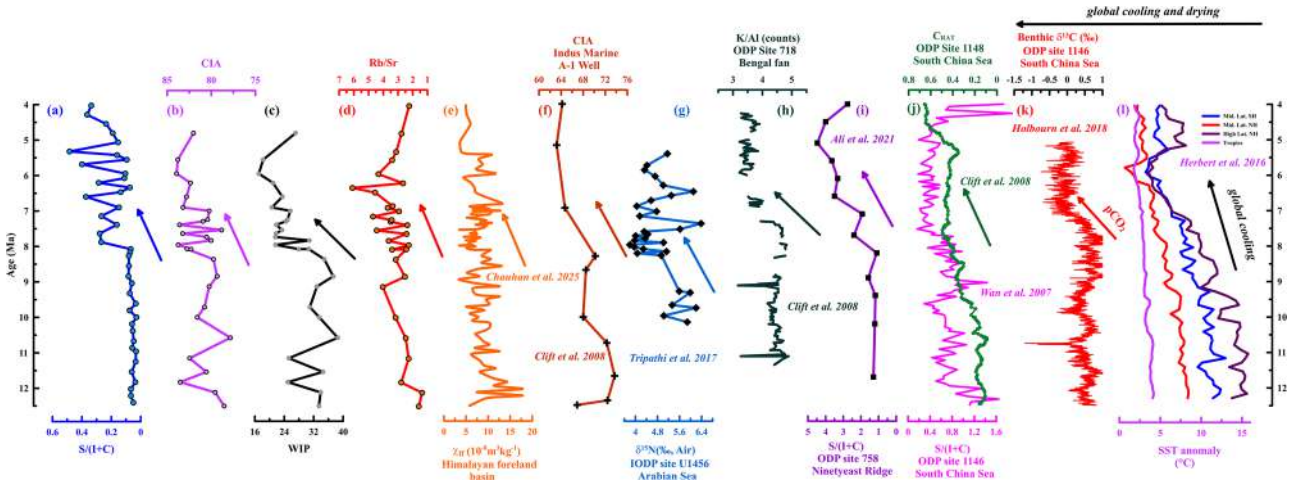

Fig. 4 | Comparison of the South Asian monsoon proxy records. a Clay mineral ratio; **b**, **c** chemical weathering indices (CIA and WIP); **d** Rb/Sr ratio of the present study; **e** low-field magnetic susceptibility at the TS section from the HFB[22]; **f** variation in CIA at site Indus Marine A-1 well from the Arabian Sea[73]; **g** variation in nitrogen isotopic record at IODP site U1456 site from the Arabian Sea[93]; **h** K/Al counts of ODP site 718 of Bengal Fan[73]; **i** S/(I + C) ratio at ODP site 758 from the Ninety East Ridge[10]; **j** The S/(I + C) ratio[23] of ODP site 1146 and variation in chemical weathering index C_{RAT} at site ODP site 1148 from the South China Sea[73]; **k** Benthic carbon isotopic record compiled from ODP site 1146 from South China Sea[94]; **l** Stacked records of sea surface temperature (SST) anomalies derived from $U^{37}_{k'}$ data, illustrating trends across the tropics, midlatitudes and high northern latitudes[88].

study, can act as a chemical weathering proxy and hence monitor monsoon intensity variation with high ratios indicate more chemical weathering in the source region.

The geochemical composition of clastic sediments is significantly affected by chemical weathering processes[33]. The depletion of alkaline elements during weathering can be quantitatively assessed with relative ease. Consequently, weathering indices such as the CIA and WIP have been proposed to evaluate the extent of chemical weathering in the source region of the sediments[33,34]. Hence, the CIA and WIP quantifies the degree of chemical weathering and provides insights into paleoclimatic conditions. Elevated CIA and low WIP values indicate pronounced chemical weathering, whereas lower CIA and higher WIP values suggest dominant physical erosion[33,34]. Additionally, enhanced chemical weathering leads to the rapid leaching of Sr relative to Rb[33], resulting in increased Rb/Sr ratios with increase chemical weathering. Therefore, CIA, WIP and Rb/Sr ratios, along with the S/(I + C) ratio, can collectively serve as proxies for assessing chemical weathering and hence South Asian monsoon variability in the present study.

In high-relief terrains such as the NW Himalaya, intense precipitation under warm and wet climatic conditions typically drives physical weathering to dominate over chemical alteration, even when climatic settings would otherwise favor enhanced chemical weathering[70]. Steep slopes promote rapid surface runoff, reducing water-rock interaction time and thereby suppressing geochemical processes such as hydrolysis, oxidation and carbonation[71–73]. This effect is especially pronounced in the NW Himalaya, where steep topography coincides with heavy monsoonal rainfall[18]. Under such conditions, intense rainfall enhances mechanical denudation and detrital transport while inhibiting chemical transformation of clastic sediments, whereas cooler and drier intervals tend to reverse this balance by favoring chemical alteration[16,73]. As the source of the present study region lies in the high-relief Himalaya and high-rainfall zone[18], sediments deposited between 12.5 and 8 Ma are characterized by clay mineral assemblages dominated by illite and chlorite with low S/(I + C) ratios (Fig. 2b, d, e), indicating intense physical erosion and limited chemical weathering in the source area. This interpretation is supported by geochemical indices, as CIA and Rb/Sr values (Fig. 4b, d) reflect subdued chemical alteration alongside strong physical erosion, while WIP trends closely follow illite and chlorite abundances and suggest weak chemical weathering in the source region during this period (Fig. 4c). Collectively, these proxies indicate that from 12.5 to 8 Ma, high physical erosion and weak chemical weathering prevailed, likely in response to a strengthened South Asian monsoon. From 8 to 4 Ma, the clay mineral record shifts toward higher smectite content and rising S/(I + C) ratios (Fig. 2a, e), signaling a reduction in mechanical erosion and relatively enhanced chemical alteration. Corresponding CIA, WIP and Rb/Sr values confirm elevated chemical weathering and diminished physical erosion (Fig. 4b–d). Taken together, these clay mineral and geochemical records suggest that during 8 to 4 Ma, reduced mechanical erosion and increased chemical weathering occurred, reflecting a weakened South Asian monsoon[10,20,73].

The Late Miocene evolution of the Asian monsoon climate was predominantly influenced by global cooling[74] and the uplift of the HTP[13]. In particular, the uplift and expansion of the Tibetan Plateau, as indicated by climate models, played a significant role in intensifying the Asian monsoon system by influencing atmospheric circulation[13,75,76]. The Himalayan paleogeographic evolution combined with provenance quantitative analysis of the Bengal fan sediments, suggested that significant uplift of the Himalayan Mountain belt probably began no earlier than the Miocene[77]. However, tectonic activity in the region persisted throughout the Miocene, characterized by gradual west-to-east deformation, ultimately contributing to the formation of the Himalayan Mountain ranges, reaching near-modern elevations by the Late Miocene[78]. Muscovite Ar-Ar thermochronometric studies suggested that the rapid exhumation of the Greater Himalaya began around 20–30 Ma in the western Himalaya and approximately at 10–25 Ma in the central Himalaya with exhumation rates declining near ~17 Ma and again during 6–8 Ma[79]. Detrital zircon fission-track records from the Miocene-Pliocene Siwalik Group indicate unroofing of the Central Himalaya near ~16 Ma, reflecting sustained rather than accelerated exhumation[80]. Detrital apatite fission-track analyses of modern river sediments and Bengal Fan deposits similarly suggest relatively constant exhumation rates since ~13 Ma[77]. A progressive southward migration of Himalayan tectonics, with exhumation of the Higher Himalaya slowing by ~17 Ma, followed by surface exposure of the non-metamorphosed Inner Lesser Himalaya ~9 Ma and eventual exhumation of the metamorphosed Lesser Himalayan Crystalline Series by ~6 Ma[81].

In addition, the bedrock erosion rates of the Higher and Lesser Himalayan rocks, Kumaun-Garhwal regions of the NW Himalaya, which represent the source rocks of the studied section of the TS Sub-Himalayan rocks (Supplementary Table 5)[82–86]. These records clearly suggest that the bedrock erosion rates were mostly less than 0.5 mm/yr and as low as 0.2 mm/yr around ~8 Ma or in the Late Miocene in the Kumaun-Garhwal

regions[84–86]. Even in the entire Himalayan orogen and NW Himalaya, the bedrock erosion rates for the upper regions of the Higher Himalayas were less than 1.0 mm/yr from ~10 to 4 Ma[82] or ~0.4 ± 0.1 mm/yr from ~13 to 2 Ma[83], which contributed mostly to the deposition of Sub-Himalayan rocks[15,53,54]. The only unit that exhumed relatively higher rates (average ~2.9 mm/yr) during 11-4 Ma lies in the NW Himalaya, however, still these erosion rates were nearly half the rate of ~4.5 mm/yr that existed at ~14-13 Ma or ~0.9-0.3 Ma in the Kumaun-Garhwal regions or during ~23–19 Ma for the entire NW Himalayan regions (Supplementary Table 5)[83–85]. Furthermore, the only phase of rapid erosion occurred during the Plio-Quaternary, following the Middle Miocene, in the NW Himalaya (Supplementary Table 5)[82,83,86]. The Late Miocene (~8 Ma) phase of Himalayan evolution was marked by a pronounced slowdown in tectonically driven erosion, coincident with the initial uplift of the Inner Lesser Himalaya and reorganization of drainage networks[81]. This reduced exhumation facilitated longer sediment–water interaction times, enhancing silicate weathering and contributing to atmospheric CO_2 drawdown.

The climatic transition around ~8 Ma, hence, is best understood as a product of global cooling, which has been proven to act as the forcing behind the widespread weakening of the South Asian monsoon and the concurrent shift from intense physical erosion to more pronounced chemical weathering[10,87]. This shift of weathering regime is evidenced by the coeval rise in S/(I + C) ratios, elevated CIA, Rb/Sr and decreased WIP indices across the HFB (Fig. 4a-d). Magnetic susceptibility records from the same HFB section document a pronounced shift at ~8 Ma, characterized by reduced values of concentration-dependent magnetic parameters[22] (Fig. 4e). This change is interpreted as a weakening of the Indian monsoon, likely also driven by global cooling[22]. Multiple regional and global datasets support this linkage, emphasizing that the ~8 Ma transition reflects a climate-driven[88–94]. The global sea surface temperature (SST) records from various DSDP, ODP and IODP sites also indicate synchronous cooling in both hemispheres during the Late Miocene (Fig. 4l)[88]. The carbon and oxygen isotopic records of fossil gastropods from the North China Loess[11], along with geochemical and magnetic data from Chinese loess deposits[89] and plant wax isotope records from eolian sediments in the North Pacific[90], collectively suggest a marked decline in temperature, supporting evidence for global cooling around 8 Ma. Records from the Arabian Sea, Bay of Bengal and South China Sea suggest reduced precipitation intensity and a stepwise shift toward more arid and seasonal climates linked with global cooling[10,87,91,92,95]. In the Arabian Sea, geochemical[73] (Fig. 4f) and nitrogen isotopic[93] (Fig. 4g) records indicate a persistently weak South Asian monsoon since the Late Miocene, with no intensification at ~8 Ma. In the South China Sea, clay mineral assemblages and bulk mineralogical composition[23,73] (Fig. 4j) show a marked decline in chemical alteration after ~8 Ma, suggesting that weakened monsoonal runoff curtailed silicate weathering flux. Furthermore, benthic foraminiferal $\delta^{13}C$ records from the South China Sea document a major cooling event and Antarctic ice-sheet expansion at ~7.9 Ma[94] (Fig. 4k). In contrast, records from the Bay of Bengal indicate intensified chemical weathering during the same interval, reflected by low elemental K/Al ratios[73] (Fig. 4h) and enhanced clay mineral alteration indicating chemical weathering[10] (Fig. 4i), overall reduced monsoon intensity with shift in monsoonal precipitation locus from north-west dominated to north-east dominated in the northern India[4,10,73,87,96]. These opposing trends suggest that while overall monsoon precipitation weakened, spatially variable hydrological responses amplified by global cooling drove enhanced chemical weathering in basins with high runoff efficiency (e.g., Bay of Bengal) but suppressed weathering in more aridifying regions like the source region of the Arabian Sea sediments[73]. Similar responses are also observed across the South China Sea, where provenance transitions[92] and palynological reorganizations[97] coincide with this cooling interval. The intensification of the East Asian winter monsoon in the Late Miocene also linked with declining atmospheric CO_2[98]. To strengthen this interpretation, we additionally incorporate the recently synthesized high-elevation record from the Zhada Basin in western Tibet, which captures late Miocene South Asian summer monsoon variations. This record suggests a pronounced weakening of the Asian summer monsoon around ~7.2 Ma, primarily attributed to global climate forcing[99].

The carbon isotope composition ($\delta^{13}C$) of sedimentary organic matter and carbonates serves as a robust proxy for reconstructing the relative contributions of C_3 and C_4 vegetation within catchment areas, provided that soil-respired CO_2 remains sufficiently elevated to minimize the influence of atmospheric CO_2 diffusion[100]. Temporal fluctuations in $\delta^{13}C$ can therefore be used to infer vegetation dynamics, with more negative values indicating C_3 dominance and enriched values reflecting enhanced C_4 input, due to the distinct photosynthetic fractionation mechanisms of these plant groups: C_3 plants strongly discriminate against ^{13}C, producing lower $\delta^{13}C$ values, whereas C_4 plants yield comparatively higher $\delta^{13}C$ owing to reduced fractionation. Within the studied section, $\delta^{13}C$ depletion from 12.5 to 8 Ma reflects a landscape dominated by C_3 flora (Fig. S4a), whereas enrichment after 8 Ma indicates progressive C_4 expansion[22]. The transition from a C_3 tree-dominated ecosystem to predominantly C_4 grassland communities around ~8 Ma (Figure. S4b), initially linked to intensification of the South Asian monsoon[101], is now widely reinterpreted as a response to progressive Late Miocene monsoon weakening, expressed through reduced rainfall, greater seasonality and associated aridification. This reinterpretation is supported by multiple lines of evidence, including enhanced weathering intensity, elevated $\delta^{18}O$ values in soil carbonates and the ecological preference of C_4 grasses for environments characterized by pronounced dry-seasonality and reduced rainfall[20,102,103]. Isotopic archives from the western Siwaliks document a pronounced C_4 expansion between ~8.5 and 6.5 Ma[104] (Fig. S4c), with post-7 Ma proliferation across the western Himalaya reflecting declining monsoon-driven precipitation but increased seasonality[20] (Figure. S4d). However, stable $\delta^{13}C$ profiles from the Kameng section (eastern Himalaya) indicate continued C_3 dominance under persistently humid, less seasonal regimes due to its proximity to oceanic moisture sources; however, clay mineral and geochemical weathering proxies from the same section suggest reduced effective precipitation and weakening monsoon intensity around 8 Ma, likely linked to global cooling[20]. This pattern is further supported by $\delta^{13}C$ of n-alkanes (C_{27} - C_{31}) from Surai Khola (Nepalese Siwaliks), which record a progressive shift from C_3 to C_4 dominance between 8 and 5 Ma[105] (Fig. S4e), consistent with Neupane's evidence for a stepwise expansion beginning ~8.5 Ma and accelerating after ~5.2 Ma[106] (Fig. S4e). These molecular biomarker records are widely recognized as robust indicators of C_4 vegetation proliferation[107,108]. Further west, a ~ 6‰ $\delta^{13}C$ increase in plant wax n-alkanes from the Indus Fan[103] (Fig. S4f) and comparable shifts from the Bengal Fan[108] (Fig. S4g) highlight substantial Late Miocene C_4 expansion, likely accentuated by concurrent global cooling, which weakened summer monsoon convection, amplified aridification and increased wildfire frequency across the Indian subcontinent, further facilitating C_4 proliferation[109]. High-resolution benthic $\delta^{13}C$ record of ODP Site 1146 (South China Sea) likewise documents the Late Miocene cooling driven by carbon-cycle reorganizations and declining precipitation, conditions that weakened monsoon strength, intensified climatic seasonality and promoted widespread establishment of C_4 grasses[94] (Fig. S4h).

In summary, multiproxy weathering records derived from clay mineral assemblages, geochemical compositions and vegetation indicators from the HFB, integrated with climatically coherent yet regionally contrasting continental and marine weathering signals from the Arabian Sea, Bay of Bengal and South China Sea, demonstrate a definitive reorganization of the South Asian monsoon during the Late Miocene. Around ~8 Ma, the system underwent a pronounced but potential multi-cause transition toward reduced tectonic activity, change in monsoon-driven runoff, increased aridification and increased seasonality. This shift was likely influenced by driven by the coupled influence of HTP uplift and global cooling[70,73,110]. Although alternative mechanisms such as change in erosion efficiency or subtle provenance adjustments may also have contributed to the observed geochemical and mineralogical trends. This reorganization is corroborated by synchronous declines in marine sediment flux, clay mineral transitions

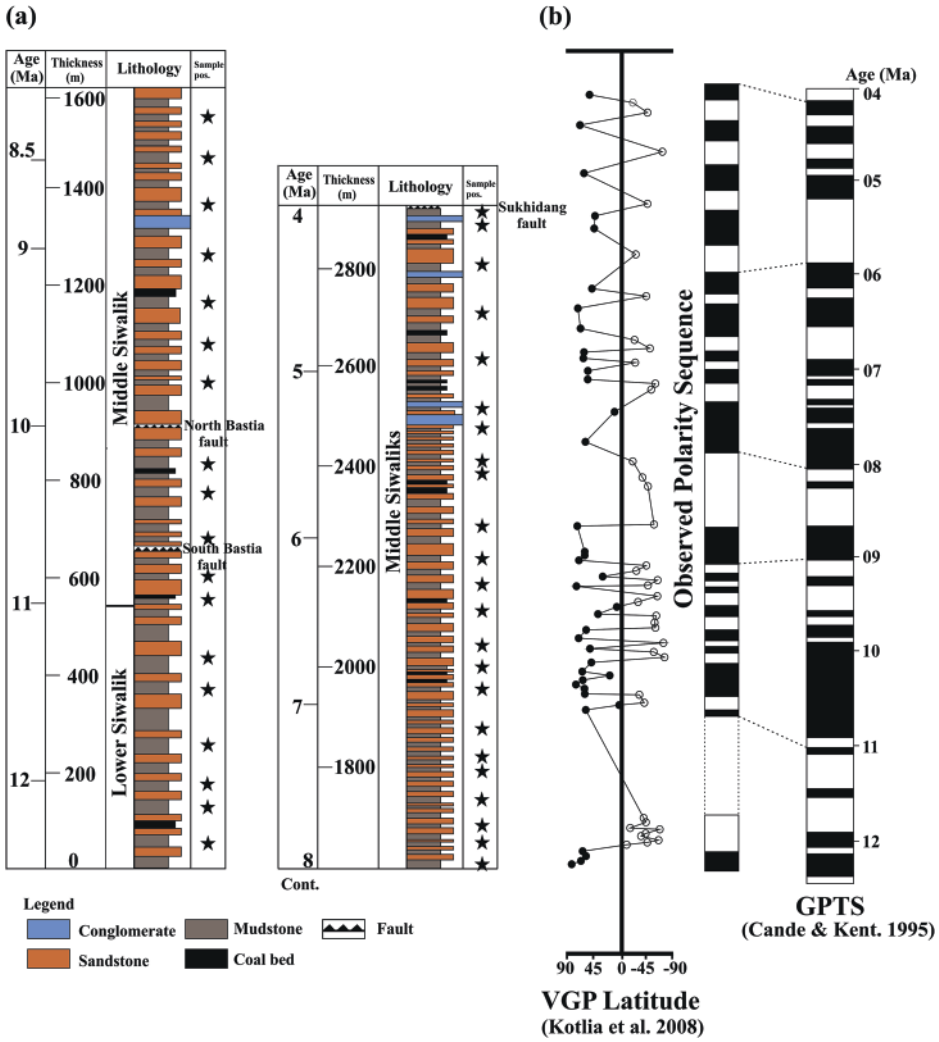

Fig. 5 | Lithostratigraphy and magnetostratigraphy of the TS section of the HFB and correlation to the geomagnetic polarity timescale (GPTS). a Modified Litholog[111]; **b** virtual geomagnetic pole (VGP) latitude and paleomagnetic polarity for the TS section[111] and correlation to the GPTS[124].

and isotopic signatures across the Indo-Pacific, reflecting basin-wide hydrological adjustments to both tectonic and climatic forcing. Hence, the change in exhumation rates of the HTP and intensified chemical weathering during the Late Miocene collectively indicate, rather than definitively prove, that both tectonics and global climate forcing as the primary drivers of monsoon weakening and environmental transformation. We acknowledge that distinguishing climatic weakening from tectonically driven erosion reduction remains challenging, and future work integrating higher-resolution provenance tracers, thermochronology and climate-model simulations will be essential to further constrain the mechanisms behind the ~8 Ma transition.

Methods

In this study, we select mudstone samples from the TS section with continuous Neogene deposition dated by magnetostratigraphy[111] (Fig. 1b). The TS section (29°04′53″N, 80°04′41″E to 29°09′47″N, 80°04′38″E) is 3000 m thick (Fig. 5a). The Lower and Middle Siwalik are exposed in this section (Fig. 1b). The exposed portion of the Lower Siwalik is 560 m thick and is comprised of dark to pale brown, purple, compact mudstone that is interbedded with fine-grained sandstone[111,112]. Whereas about 2400 m thick sediments of overlying Middle Siwalik are characterized by medium to coarse-grained sandstones and subordinate greyish to brown mudstones along with conglomerate[111,112]. The previous detailed magnetostratigraphic study in this section suggests that sediments of Lower and Middle Siwalik were deposited during 12.5–11 Ma and 11–4 Ma, respectively[111] (Fig. 5b). Several faults traverse this section, i.e., the Bastia fault, Tanakpur fault, Sukhidang fault and Kalaunia fault (Fig. 1b).

Major elements analysis

At the Inter-University Accelerator Center (IUAC), Ministry of Earth Sciences, India, the major elements in the 28 mudstone samples were analyzed using the Axios Max, PANalytical sequential wavelength dispersive X-ray fluorescence spectrometer (WD-XRF). In the first step, the samples were powdered to a particle size of <63 μm using a tungsten ball mill available at the Birbal Sahni Institute of Palaeosciences (Lucknow, India). The homogenized powdered samples (~20 mg) were treated with 10% HCl to remove carbonate phases and this step was repeated until all carbonate fractions were completely dissolved. This is followed by triple rinsing with MQ to eliminate residual acid. Residual organic matter was subsequently removed by ashing the samples at 550 °C for four hours in a controlled-temperature muffle furnace. A 6.4 g of treated sample was mixed with 1.6 g of boric acid to make a pellet using a Kameyo powder press machine with a 40-ton load. The WD-XRF technique determined the concentrations of ten major oxides SiO_2, Al_2O_3, Fe_2O_3, MgO, CaO, Na_2O, K_2O, TiO_2, P_2O_5 and MnO. To ensure quality, standard JSD-2 and GXR-2 were also analyzed. The analytical accuracy and precision were less than 2%. The total loss of ignition (LOI) was determined after heating the samples for 6 h at 950 °C. The concentrations of major elements were reported as weight percentages. The CIA[33] and WIP[34] have been used to interpret the chemical weathering intensity of the TS section sediments (Fig. 4b, c). The values of CIA and WIP

have been derived by using the following Eqs. (1) and (2), respectively:

$$CIA = \frac{Al_2O_3}{(Al_2O_3 + K_2O + CaO^* + Na_2O)} X100 \quad (1)$$

$$WIP = \left(2X\frac{Na_2O}{0.35} + 2X\frac{K_2O}{0.25} + \frac{MgO}{0.90} + \frac{CaO^*}{0.70}\right) X100 \quad (2)$$

Here, CaO* represents the calcium oxide component associated exclusively with silicate minerals.

Trace and REEs analysis

Several trace and REEs are widely used to investigate shifts in provenance and source rock composition[47,48]. Thirty samples were ground to a particle size of <63 µm with a tungsten ball mill for analyzing the geochemical composition. To remove carbonate content, samples were treated with 10% HCl and, in the next step, heated at 550 °C for 4 h in an oven to remove organic content. About 30 mg of the treated sample was dissolved in a triple acid mixture of HF-HNO_3-HCl in 15 ml Savillex vial. The analysis of trace elements and REEs was carried out by ICP-MS (Agilent, 7700 series) at the Geochemistry Laboratory of Birbal Sahni Institute of Palaeosciences, Lucknow. The analytical accuracy and precision were maintained through the various duplicates and USGS standards (RGM-2 and GSP-2) and were better than 5%. All trace element and rare earth element (REE) concentrations in our study are reported in µg/g.

Clay mineral extraction and identification

In this study, 41 samples were used for clay mineral assemblage analysis in the Lower and Middle Siwalik of the TS section. Typically, data samples were uniformly distributed across the TS section, with a temporal resolution of ~ 0.2 million years. For palaeoclimate assessment based on clay mineral and geochemical composition, we select only mudstone samples because clay minerals found in siltstones and sandstones may form through authigenesis during the early stages of diagenesis[113].

The paleoclimatic evolution since the Neogene in the HFB was derived only from the analysis of mudstone samples. Before separating the clay fraction (<2 µm), selected samples were treated with 10% acetic acid (CH_3COOH) and 20% hydrogen peroxide (H_2O_2) to remove carbonate and organic fraction, respectively. From treated samples, clay fractions were separated by a centrifuge-based Atterberg method and oriented glass mounts in an ethylene glycol state were prepared. The X-ray diffraction (PANalytical, model- X'PERT^3 Powder) was used to identify the clay minerals. The XRD analytical conditions at the time of analysis were as follows: radiation CuKa, 40 mA, 45 kV and the scanning range was 2–40°(2θ). The clay mineral identification was based on the positioning of the (001) series of basal reflections on the XRD pattern[114]. A semi-quantitative analysis of peak areas for the main clay mineral groups (smectite includes mixed smectite and illite -17 Å, illite-10 Å, and kaolinite/chlorite-7 Å) was conducted on glycolated samples[115] (Fig. S5). The relative proportions of kaolinite and chlorite were estimated from the ratio of peak areas at 3.57 Å and 3.54 Å, respectively[116] (Fig. S5). The illite crystallinity is used to assess the illite crystal structure[117–120] and intensity of hydrolysis[121]. High values of illite crystallinity indicate poorly crystallized illite formed under strong hydrolyzing conditions, while low values suggest well-crystallized illite formed under weak hydrolysis conditions[122,123].

Data Availability

All data generated during this study are included in the supplementary information files.

Code availability

This study did not involve the use of any code or script.

Received: 17 August 2025; Accepted: 4 December 2025;
Published online: 23 December 2025

References

1. Wang, P. Cenozoic deformation and the history of sea-land interactions in Asia. *Geophys. Monogr. Ser.* **149**, 1–22 (2004).
2. Harris, N. The elevation history of the Tibetan Plateau and its implications for the Asian monsoon. *Palaeogeogr. Palaeoclimatol. Palaeoecol.* **241**, 4–15 (2006).
3. Molnar, P., England, P. & Martinod, J. Mantle dynamics, uplift of the Tibetan Plateau, and the Indian monsoon. *Rev. Geophys.* **31**, 357–396 (1993).
4. Clift, P. D., Wan, S. & Blusztajn, J. Reconstructing chemical weathering, physical erosion and monsoon intensity since 25 Ma in the northern South China Sea: a review of competing proxies. *Earth Sci. Rev.* **130**, 86–102 (2014).
5. Zheng, H. et al. Formation of the first bend in the late eocene gave birth to the modern yangtze river, china. *Geol* **49**, 35–39 (2021).
6. Zachos, J. et al. Trends, rhythms, and aberrations in global climate 65Ma to present. *Science* **292**, 686–693 (2001).
7. Sun, X. & Wang, P. How old is the Asian monsoon system? Palaeobotanical records from China. *Palaeogeogr. Palaeoclimatol. Palaeoecol.* **222**, 181–222 (2005).
8. Guo, Z. T. et al. A major reorganization of Asian climate by the early Miocene. *Climate* **4**, 153–174 (2008).
9. Kroon, D., Steens, T. & Troelstra, S. R. Onset of monsoonal related upwelling in the western Arabian sea as revealed by planktonic foraminifers 1. *Proc. Ocean Drill. Program Sci. Res.* **1**, 257–263 (1991).
10. Ali, S., Hathorne, E. C. & Frank, M. Persistent provenance of South Asian monsoon-induced silicate weathering over the past 27 million years. *Paleoceanogr. Paleoclimatol.* **36**, e2020PA003909 (2021).
11. Licht, A. Asian monsoons in a late Eocene greenhouse world. *Nature* **513**, 501–506 (2014).
12. Prell, W. L. & Kutzbach, J. E. Sensitivity of the Indian monsoon to forcing parameters and implications for its evolution. *Nature* **360**, 647–652 (1992).
13. An, Z. S. et al. Evolution of Asian monsoon and phased uplift of the Himalayas-Tibetan plateau since late Miocene times. *Nature* **411**, 62–66 (2001).
14. Ranjan, N. & Banerjee, D. M. Central Himalayan crystallines as the primary source for the sandstone–mudstone suites of the Siwalik Group: new geochemical evidence. *Gondwana Res.* **16**, 687–696 (2009).
15. Jalal, P. & Ghosh, S. K. Provenance of the Late Neogene Siwalik sandstone, Kumaun Himalayan Foreland Basin: constraints from the metamorphic rank and index of detrital rock fragments. *J. Earth Syst. Sci.* **121**, 781–792 (2012).
16. Ali, S. et al. Provenance, weathering, and paleoclimatic records of the Pliocene-Pleistocene sequences of the Himalayan foreland basin, NW Himalaya. *Arab. J. Geosci.* **14**, 198 (2021).
17. Singh, P. & Patel, R. C. Mio-Pliocene exhumation of the hinterland and sediments provenance of the Neogene strata from Kumaun Himalaya of northwest India: insights from detrital fission-track thermochronology. *Geol. J.* **59**, 29–45 (2024).
18. Bookhagen, B. & Burbank, D. W. Topography, relief, and TRMM-derived rainfall variations along the Himalaya. *Geophys. Res. Lett.* **33**, 26037 (2006).
19. Karim, A. & Veizer, J. Water balance of the Indus River Basin and moisture source in the Karakoram and western Himalayas: implications from hydrogen and oxygen isotopes in river water. *J. Geophys. Res. Atmos.* **107**, 253 (2002).
20. Vögeli, N. et al. Lateral variations in vegetation in the Himalaya since the Miocene and implications for climate evolution. *Earth Planet. Sci. Lett.* **471**, 1–9 (2017).
21. Chauhan, M. M. et al. Silicate weathering linked with global climate change along the Mid-Pleistocene transition: a record from the Himalayan foreland Basin, India. *Catena* **241**, 108047 (2024).

22. Chauhan, M. M. et al. Reconstruction of the Late Miocene climate record in the Himalayan foreland Basin: the impact of Himalayan uplift and monsoon dynamics. *J. Asian Earth Sci.* **280**, 106445 (2025).
23. Wan, S., Li, A., Clift, P. D. & Stuut, J. B. Development of the East Asian monsoon: mineralogical and sedimentologic records in the northern South China Sea since 20 Ma. *Palaeogeogr. Palaeoclimatol. Palaeoecol.* **254**, 561–582 (2007).
24. Miao, Y. et al. What controlled Mid–Late Miocene long-term aridification in Central Asia? Global cooling or Tibetan Plateau uplift: a review. *Earth Sci. Rev.* **112**, 155–172 (2012).
25. Lu, H. & Guo, Z. Evolution of the monsoon and dry climate in East Asia during late Cenozoic: a review. *Sci. China Earth Sci.* **57**, 70–79 (2014).
26. Burbank, D. W. et al. Bedrock incision, rock uplift and threshold hillslopes in the northwestern Himalayas. *Nature* **379**, 505–510 (1996).
27. Najman, Y., Johnson, K., White, N. & Oliver, G. Evolution of the Himalayan foreland basin, NW India. *Basin Res.* **16**, 1–24 (2004).
28. Garzanti, E. The Himalayan Foreland Basin from collision onset to the present: a sedimentary–petrology perspective. *Geol. Soc. Spec. Publ.* **483**, 65–122 (2019).
29. Najman, Y., Pringle, M., Godin, L. & Oliver, G. Dating of the oldest continental sediments from the Himalayan foreland basin. *Nature* **410**, 194–197 (2001).
30. Singh, B. P. Evolution of the Paleogene succession of the western Himalayan foreland basin. *Geosci. Front.* **4**, 199–212 (2013).
31. Pilgrim, G. E. Notices of new mammalian genera and species from the Tertiaries of India. *Rec. Geol. Surv. India* **40**, 63–71 (1910).
32. Tandon, S. K. The Himalayan foreland: Focus on Siwalik basin. Sedimentary basins of India. 171–201 (Springer, 1991).
33. Nesbitt, H. & Young, G. M. Early Proterozoic climates and plate motions inferred from major element chemistry of lutites. *Nature* **299**, 715–717 (1982).
34. Parker, A. An index of weathering for silicate rocks. *Geol. Mag.* **107**, 501–504 (1970).
35. Rudnick, R. L. & Gao, S. Composition of the continental crust. *Treat. Geochem.* **3**, 1–64 (2003).
36. Taylor, S. R. & McLennan, S. M. *The Continental Crust: its Composition and Evolution* (Stony Brook University, 1985).
37. Fang, X. et al. Paleogene global cooling–induced temperature feedback on chemical weathering, as recorded in the northern Tibetan Plateau. *Geology* **47**, 992–996 (2019).
38. Ye, C. et al. Evolution of Paleogene weathering intensity in the Qaidam Basin, northeastern Tibetan Plateau: insights from clay geochemistry. *Catena* **213**, 106162 (2022).
39. Shu, W. et al. Terrigenous provenance of late Oligocene–Miocene sediments in the central basin of the South China Sea and its implications for chemical weathering and climate change. *Mar. Geol.* **462**, 107098 (2023).
40. Lenz, N. et al. Provenance of clay-sized detrital sediments in the North Sea and the Skagerrak region based on radiogenic Nd-Sr-Hf isotopes and clay mineral compositions: assessing the impact of coastal and seabed erosion. *Front. Mar. Sci.* **11**, 1416519 (2024).
41. Dong, H. & Song, Y. Clay mineralogy and its application to paleoenvironmental reconstruction. *Mar. Geol. Quat. Geol.* **29**, 119–130 (2010).
42. McLennan, S. M. & Taylor, S. R. Sedimentary rocks and crustal evolution: tectonic setting and secular trends. *J. Geol.* **99**, 1–21 (1991).
43. Cullers, R. L. The controls on the major and trace element variation of shales, siltstones, and sandstones of Pennsylvanian-Permian age from uplifted continental blocks in Colorado to platform sediment in Kansas, USA. *Geochim. Cosmochim. Acta* **58**, 4955–4972 (1994).
44. Armstrong-Altrin, J. S. et al. Geochemistry of beach sands along the western Gulf of Mexico, Mexico: implication for provenance. *Geochemistry* **72**, 345–362 (2012).
45. McLennan, S. M. Rare earth elements in sedimentary rocks: influence of provenance and sedimentary processes. *Geochem. Mineral. Rare Earth Elements* **21**, 169–200 (2018).
46. Armstrong-Altrin, J. S., Lee, Y. I., Verma, S. P. & Ramasamy, S. Geochemistry of sandstones from the Upper Miocene Kudankulam Formation, southern India: implications for provenance, weathering, and tectonic setting. *J. Sediment. Res.* **74**, 285–297 (2004).
47. McLennan, S. M., Hemming, S., McDaniel, D. K. & Hanson, G. N. Geochemical approaches to sedimentation, provenance, and tectonics. In *Processes Controlling the Composition of Clastic Sediments*. https://doi.org/10.1130/SPE284 (GSA, 1993).
48. Condie, K. C. Chemical composition and evolution of the upper continental crust: contrasting results from surface samples and shales. *Chem. Geol.* **104**, 1–37 (1993).
49. Wronkiewicz, D. J. & Condie, K. C. Geochemistry and mineralogy of sediments from the Ventersdorp and Transvaal Supergroups, South Africa: cratonic evolution during the early Proterozoic. *Geochim. Cosmochim. Acta* **54**, 343–354 (1990).
50. Cullers, R. L. Implications of elemental concentrations for provenance, redox conditions, and metamorphic studies of shales and limestones near Pueblo, CO, USA. *Chem. Geol.* **191**, 305–327 (2002).
51. Derry, L. A. & France-Lanord, C. Neogene Himalayan weathering history and river $^{87}Sr/^{86}Sr$: impact on the marine Sr record. *Earth Planet. Sci. Lett.* **142**, 59–74 (1996).
52. Quade, J., Roe, L., DeCelles, P. G. & Ojha, T. P. The late Neogene $^{87}Sr/^{86}Sr$ record of lowland Himalayan rivers. *Science* **276**, 1828–1831 (1997).
53. Galy, A. & France-Lonard, C. Higher erosion rates in the Himalaya: geochemical constraints on riverine fluxes. *Geology* **29**, 23–26 (2001).
54. Jalal, P., Ghosh, S. K. & Sundriyal, Y. P. Detrital modes of Late Neogene Siwalik Sandstone of the Ramganga Sub-basin, Kumaun Sub-Himalaya: Implication for the source area tectonic history. *Him. Geol.* **32**, 123–135 (2011).
55. Jalal, P., Ghosh, S. K. & Sundriyal, Y. P. Climatic phases and its effect in the derivation and deposition of Himalayan foreland basin. Climate Change & Himalayan Ecosystem-Indicator, Bio & Water Resources (Springer, 2013).
56. Singh, B. P., Pawar, J. S. & Karlupia, S. K. Dense mineral data from the northwestern Himalayan foreland sedimentary rocks and recent river sediments: evaluation of the hinterland. *J. Asian Earth Sci.* **23**, 25–35 (2004).
57. Thiry, M. Palaeoclimatic interpretation of clay minerals in marine deposits: an outlook from the continental origin. *Earth Sci. Rev.* **49**, 201–221 (2000).
58. Chamley, H. *Clay Mineralogy* (Springer, 1989).
59. Liu, Z. et al. Clay mineral assemblages in the northern South China Sea: implications for East Asian monsoon evolution over the past 2 million years. *Mar. Geol.* **201**, 133–146 (2003).
60. Huyghe, P. et al. Significance of the clay mineral distribution in fluvial sediments of the Neogene to Recent Himalayan Foreland Basin (west-central Nepal). *Basin Res* **23**, 332–345 (2011).
61. Chen, Q., Liu, Z. & Kissel, C. Clay mineralogical and geochemical proxies of the East Asian summer monsoon evolution in the South China Sea during Late Quaternary. *Sci. Rep.* **7**, 42083 (2017).
62. Ye, G. L. et al. Effect of Quaternary transgression and regression on the engineering properties of Shanghai soft clays. *Eng. Geol.* **239**, 321–329 (2018).
63. Liu, Y. et al. Paleoclimate change since the Miocene inferred from clay-mineral records of the Jiuquan Basin, NW China. *Palaeogeogr. Palaeoclimatol. Palaeoecol.* **550**, 109730 (2020).

64. Chamley, H. Clay mineral diagenesis. In *Quantitative diagenesis: Recent developments and applications to reservoir geology* (eds Parker, A. & Sellwood, B. W.) (Springer, 1994).
65. Weaver, C. E. *Clays, muds, and shales* (Elsevier, 1989).
66. Ahn, J. H. & Peacor, D. R. Transmission and analytical electron microscopy of the smectite-to-illite transition. *Clays Clay Min.* **34**, 165–179 (1986).
67. Hower, J., Eslinger, E. V., Hower, M. E. & Perry, E. A. Mechanism of burial metamorphism of argillaceous sediment: 1. Mineralogical and chemical evidence. *Geol. Soc. Am. Bull.* **87**, 725–737 (1976).
68. Nadeau, P. H., Wilson, M. J., McHardy, W. J. & Tait, J. M. Interstratified clays as fundamental particles. *Science* **225**, 923–925 (1984).
69. Aoyagi, K. & Kazama, T. Transformational changes of clay minerals, zeolites and silica minerals during diagenesis. *Sedimentology* **27**, 179–188 (1980).
70. Exnicios, E. M., Carter, A., Najman, Y. & Clift, P. D. Late Miocene unroofing of the Inner Lesser Himalaya recorded in the NW Himalaya foreland basin. *Basin Res* **34**, 1894–1916 (2022).
71. Anderson, S. P. & Dietrich, W. E. Chemical weathering and runoff chemistry in a steep headwater catchment. *Hydrol. Process.* **15**, 1791–1815 (2001).
72. Maher, K. The dependence of chemical weathering rates on fluid residence time. *Earth Planet. Sci. Lett.* **294**, 101–110 (2010).
73. Clift, P. D. et al. Correlation of Himalayan exhumation rates and Asian monsoon intensity. *Nat. Geosci.* **1**, 875–880 (2008).
74. Miao, Y. et al. Miocene pollen record of KC-1 core in the Qaidam Basin, NE Tibetan Plateau and implications for evolution of the East Asian monsoon. *Palaeogeogr. Palaeoclimatol. Palaeoecol.* **299**, 30–38 (2011).
75. Tada, R., Zheng, H. & Clift, P. D. Evolution and variability of the Asian monsoon and its potential linkage with uplift of the Himalaya and Tibetan Plateau. *Prog. earth planet. sci.* **3**, 1–26 (2016).
76. Ruddiman, W. F. & Kutzbach, J. E. Forcing of late Cenozoic northern hemisphere climate by plateau uplift in southern Asia and the American West. *J. Geophys. Res. Atmos.* **94**, 18409–18427 (1989).
77. Huyghe, P. et al. Rapid exhumation since at least 13 Ma in the Himalaya recorded by detrital apatite fission-track dating of Bengal fan (IODP Expedition 354) and modern Himalayan river sediments. *Earth Planet. Sci. Lett.* **534**, 116078 (2020).
78. Song, Z. et al. The major uplift in Himalayas was no earlier than the Miocene: evidence from marine sediment record in the Bay of Bengal. *Palaeogeogr. Palaeoclimatol. Palaeoecol.* **648**, 112275 (2024).
79. Clift, P. D. Cenozoic sedimentary records of climate-tectonic coupling in the Western Himalaya. *Prog. Earth Planet. Sci.* **4**, 1–22 (2017).
80. Bernet, M. et al. Miocene to recent exhumation of the central Himalaya determined from combined detrital zircon fission-track and U/Pb analysis of Siwalik sediments, western Nepal. *Basin Res.* **18**, 393–412 (2006).
81. Najman, Y. et al. Reconstructing the exhumation history of the Lesser Himalaya, NW India, from a multitechnique provenance study of the foreland basin Siwalik Group. *Tectonics* **28**, 2506 (2009).
82. Thiede, R. C. & Ehlers, T. A. Large spatial and temporal variations in Himalayan denudation. *Earth Planet. Sci. Lett.* **371**, 278–293 (2013).
83. Thiede, R. C., Ehlers, T. A., Bookhagen, B. & Strecker, M. R. Erosional variability along the northwest Himalaya. *J. Geophys. Res. Earth Surf.* **114**, 1010 (2009).
84. Singh, P., Patel, R. C. & Lal, N. Plio-Plistocene in-sequence thrust propagation along the Main Central Thrust zone (Kumaon-Garhwal Himalaya, India): new thermochronological data. *Tectonophysics* **574**, 193–203 (2012).
85. Singh, P. & Patel, R. C. Miocene development of the Main Boundary thrust and Ramgarh thrust, and exhumation of Lesser Himalayan rocks of the Kumaun-Garhwal region, NW-Himalaya (India): Insights from fission track thermochronology. *J. Asian Earth Sci.* **224**, 104987 (2022).
86. Patel, R. C. et al. Spatiotemporal variation in exhumation of the crystallines in the NW-Himalaya, India: Constraints from Fission Track dating analysis. *Tectonophysics* **504**, 1–13 (2011).
87. Bretschneider, L. et al. Provenance and weathering of clays delivered to the Bay of Bengal during the middle Miocene: linkages to tectonics and monsoonal climate. *Paleoceanogr. Paleoclimatol.* **36**, 2020PA003917 (2021).
88. Herbert, T. D. et al. Late Miocene global cooling and the rise of modern ecosystems. *Nat. Geosci.* **9**, 843–847 (2016).
89. Guo, Z. T. et al. Onset of Asian desertification by 22 Myr ago inferred from loess deposits in China. *Nature* **416**, 159–163 (2002).
90. Jia, G., Li, Z., Peng, P. A. & Zhou, L. Aeolian n-alkane isotopic evidence from North Pacific for a Late Miocene decline of C4 plant in the arid Asian interior. *Earth Planet. Sci. Lett.* **321**, 32–40 (2012).
91. Clift, P. D. & Curtis, J. G. A revised chemical weathering and sediment provenance history for the Late Miocene to recent Laxmi Basin, Arabian Sea. *Geol. Mag.* **161**, 20 (2024).
92. Yan, Y. et al. Provenance shift of the abyssal plains in the Southwest sub-basin of the South China Sea at~ 8Ma: tectonics & climate changes implication. *Mar. Geol.* **475**, 107368 (2024).
93. Tripathi, S., Tiwari, M., Lee, J. & Khim, B. K. First evidence of denitrification vis-à-vis monsoon in the Arabian Sea since Late Miocene. *Sci. Rep.* **7**, 43056 (2017).
94. Holbourn, A. E. et al. Late Miocene climate cooling and intensification of southeast Asian winter monsoon. *Nat. comm.* **9**, 1584 (2018).
95. Zhou, P. et al. Zircon U-Pb age constraints on NW Himalayan exhumation from the Laxmi Basin, Arabian Sea. *Geochem. Geophys. Geosyst.* **23**, 2021GC010158 (2022).
96. Bretschneider, L. et al. Enhanced late Miocene chemical weathering and altered precipitation patterns in the watersheds of the Bay of Bengal recorded by detrital clay radiogenic isotopes. *Paleoceanogr. Paleoclimatol.* **36**, e2021PA004252 (2021).
97. Miao, Y. et al. Climatic or tectonic control on organic matter deposition in the South China Sea? A lesson learned from a comprehensive Neogene palynological study of IODP Site U1433. *Int. J. Coal Geol.* **190**, 166–177 (2018).
98. Zhang, Q. et al. East Asian winter monsoon intensification over the Northwest Pacific Ocean driven by late Miocene atmospheric CO2 decline. *Sci. Adv.* **10**, eadm8270 (2024).
99. Gao, P. et al. Transition of predominant regional tectonics to global climate forcing for Asian summer monsoons at~ 7.2Ma. *Geomorphology* **484**, 109840 (2025).
100. Cerling, T. E. The stable isotopic composition of modern soil carbonate and its relationship to climate. *Earth Planet. Sci. Lett.* **71**, 229–240 (1984).
101. Quade, J., Cerling, T. E. & Bowman, J. R. Development of Asian monsoon revealed by marked ecological shift during the latest Miocene in northern Pakistan. *Nature* **342**, 163–166 (1989).
102. Dettman, D. L. et al. Seasonal stable isotope evidence for a strong Asian monsoon throughout the past 10.7 my. *Geology* **29**, 31–34 (2001).
103. Feakins, S. J. et al. Miocene C4 grassland expansion as recorded by the Indus Fan. *Paleoceanogr. Paleoclimatol.* **35**, 2020PA003856 (2020).
104. Sanyal, P., Bhattacharya, S. K., Kumar, R., Ghosh, S. K. & Sangode, S. J. Mio–Pliocene monsoonal record from Himalayan foreland basin (Indian Siwalik) and its relation to vegetational change. *Palaeogeogr. Palaeoclimatol. Palaeoecol.* **205**, 23–41 (2004).
105. Quade, J., Cater, J. M., Ojha, T. P., Adam, J. & Mark Harrison, T. Late Miocene environmental change in Nepal and the northern Indian

subcontinent: stable isotopic evidence from paleosols. *Geol. Soc. Am. Bull.* **107**, 1381–1397 (1995).
106. Neupane, P. C., Gani, M. R., Gani, N. D. & Huang, Y. Neogene vegetation shift in the Nepalese Siwalik, Himalayas: a compound-specific isotopic study of lipid biomarkers. *Depos. Rec.* **6**, 192–202 (2020).
107. Uno, K. T., Polissar, P. J., Jackson, K. E. & deMenocal, P. B. Neogene biomarker record of vegetation change in eastern Africa. *Proc. Natl. Acad. Sci.* **113**, 6355–6363 (2016).
108. Polissar, P. J. et al. Hydrologic changes drove the late Miocene expansion of C4 grasslands on the Northern Indian subcontinent. *Paleoceanogr. Paleoclimatol.* **36**, 2020PA004108 (2021).
109. Karp, A. T., Uno, K. T., Polissar, P. J. & Freeman, K. H. Late Miocene C4 grassland-fire feedbacks on the Indian Subcontinent. *Paleoceanogr. Paleoclimatol.* **36**, 2020PA004106 (2021).
110. Song, Z. et al. Enhanced weathering input from South Asia to the Indian Ocean since the late Eocene. *Sci. Bull.* **68**, 305–313 (2023).
111. Kotlia, B. S., Phartiyal, B., Kosaka, T. & Bohra, A. R. Magnetostratigraphy and lithology of Miocene-Pliocene Siwalik deposits between Tanakpur and Sukhidang, southeastern Uttarakhand Himalaya, India. *Himal. Geol.* **29**, 127–136 (2008).
112. Goswami, P. K. & Deopa, T. Petrotectonic setting of the provenance of Lower Siwalik sandstones of the Himalayan foreland basin, southeastern Kumaun Himalaya, India. *Isl. Arc* **27**, e12242 (2018).
113. Gao, Y. et al. Clay mineralogy of the middle Mingshui Formation (upper Campanian to lower Maastrichtian) from the SKIn borehole in the Songliao Basin, NE China: implications for palaeoclimate and provenance. *Palaeogeogr. Palaeoclimatol. Palaeoecol.* **385**, 162–170 (2013).
114. Moore, D. M. & Reynolds, R. C. In *X-ray diffraction and the identification and analysis of clay minerals*, 2nd edn (Oxford University Press, 1997).
115. Biscaye, P. E. Mineralogy and sedimentation of recent deep-sea clay in the Atlantic Ocean and adjacent seas and oceans. *Geol. Soc. Am. Bull.* **76**, 803–832 (1965).
116. Biscaye, P. E. Distinction between kaolinite and chlorite in recent sediments by X-ray diffraction. *Am. Min.* **49**, 1281–1289 (1964).
117. Ali, S. et al. Paleoclimatic and paleoenvironmental reconstruction at Tarfaya Atlantic coastal basin (Morocco) based on clay mineral records from Upper Cretaceous to Quaternary. *Arab. J. Geosci.* **12**, 1–12 (2019).
118. Liu, Z. et al. Clay minerals in surface sediments of the Pearl River drainage basin and their contribution to the South China Sea. *Sci. Bull.* **52**, 1101–1111 (2007).
119. Petschick, R., Kuhn, G. & Gingele, F. Clay mineral distribution in surface sediments of the South Atlantic: sources, transport, and relation to oceanography. *Mar. Geol.* **130**, 203–229 (1996).
120. Ming, J. et al. Quaternary assemblage characteristic and provenance of clay minerals in the Parecevela Basin of the east Philippine Sea. *Mar. Geol. Quat. Geol.* **32**, 139–148 (2012).
121. Liu, R., Mei, X., Zhang, J. & Zhao, D. B. Characteristics of clay minerals in sediments of Hemudu area, Zhejiang, China in Holocene and their environmental significance. *China Geol.* **2**, 8–15 (2019).
122. Diekmann, B. & Wopfner, H. Petrographic and diagenetic signatures of climatic change in peri- and postglacial Karoo Sediments of SW Tanzania. *Palaeogeogr. Palaeoclimatol. Palaeoecol.* **125**, 5–25 (1996).
123. Liu, Z., Alain, T., Clemens, S. C. & Wang, P. Quaternary clay mineralogy in the Northern South China Sea (ODP Site 1146) implications for oceanic current transport and East Asian monsoon evolution. *Sci. China Earth Sci.* **46**, 1223–1235 (2003).
124. Cande, S. C. & Kent, D. V. Revised calibration of the geomagnetic polarity timescale for the Late Cretaceous and Cenozoic. *J. Geophys. Res. Solid Earth* **100**, 6093–6095 (1995).

Acknowledgements

The authors sincerely express their gratitude to the Director, Birbal Sahni Institute of Palaeosciences, for providing necessary facilities to conduct this research. Authors are thankful to IUAC for extending XRF facility funded by Ministry of Earth Sciences (MoES) under Geochronology project [MoES/P.O.(Seismic)8(09)-Geochron/2012]. Mohd Munazir Chauhan acknowledges financial support from CSIR-HRDG (File No- 09/528(0027)/2019-EMR-1) to carry out this research. VA thanks Director, WIHG, for constant encouragement for the collaborative research. We express our sincere gratitude to Ed Hathorne, GEOMAR, Kiel, Germany for his insightful suggestions and timely support during the revision process.

Author contributions

M.M.C., S.A., and A.M.K. conceived the idea and wrote the manuscript. P.K., M.K.M., P.S., B.P.S., V.A., L.S., B.P., and A.S. contributed to the framework of the manuscript and participated in the writing process. All authors contributed to manuscript preparation, interpretation, discussion and writing.

Competing interests

The authors declare no competing interests.

Additional information

Supplementary information The online version contains supplementary material available at https://doi.org/10.1038/s41612-025-01293-5.

Correspondence and requests for materials should be addressed to Sajid Ali or Ali M. Khan.